

The Kozai–Lidov Mechanism in Hydrodynamical Disks. II. Effects of binary and disk parameters

Wen Fu^{1,2}, Stephen H. Lubow³ and Rebecca G. Martin⁴

¹Department of Physics and Astronomy, Rice University, Houston, TX 77005, USA;

wf5@rice.edu

²Los Alamos National Laboratory, Los Alamos, NM 87545, USA

³Space Telescope Science Institute, Baltimore, MD 21218, USA

⁴Department of Physics and Astronomy, University of Nevada, Las Vegas, Las Vegas, NV

89154, USA

Received _____; accepted _____

ABSTRACT

Martin et al. (2014b) showed that a substantially misaligned accretion disk around one component of a binary system can undergo global damped Kozai–Lidov (KL) oscillations. During these oscillations, the inclination and eccentricity of the disk are periodically exchanged. However, the robustness of this mechanism and its dependence on the system parameters were unexplored. In this paper, we use three-dimensional hydrodynamical simulations to analyze how various binary and disk parameters affect the KL mechanism in hydrodynamical disks. The simulations include the effect of gas pressure and viscosity, but ignore the effects of disk self-gravity. We describe results for different numerical resolutions, binary mass ratios and orbital eccentricities, initial disk sizes, initial disk surface density profiles, disk sound speeds, and disk viscosities. We show that the KL mechanism can operate for a wide range of binary-disk parameters. We discuss the applications of our results to astrophysical disks in various accreting systems.

Subject headings: accretion, accretion disks – binaries: general – hydrodynamics – planets and satellites: formation

1. Introduction

Disks in binary systems may be misaligned with respect to their binary orbit planes. Alignment is expected in cases where the disk formation process itself is coplanar, such as the case of mass-exchange binaries. In that case, a coplanar gas stream originates from the inner Lagrange point of the mass-losing star and results in the formation of a coplanar disk. Coplanarity is expected if the binary forms from disk fragmentation (Bonnell & Bate 1994; Offner et al. 2010). Furthermore, coplanarity is the long term expected outcome of a misaligned disk, due to the effects of tidal dissipation in the disk (Papaloizou & Terquem 1995; Bate et al. 2000; Lubow & Ogilvie 2000; King et al. 2013).

On the other hand, disk misalignment is expected to persist for some time period in cases where the binary forms from a merger process, such as occurs with supermassive black hole (SMBH) binary systems (e.g., King & Pringle 2006). If a young binary star system accretes material after its formation process, the material is likely to be misaligned with the binary orbit and so misaligned disks may form around young stars (Bate et al. 2010). In addition, a coplanar disk may become noncoplanar due to an instability, such as radiation warping (Pringle 1996; Wijers & Pringle 1999; Ogilvie & Dubus 2001). Be/X-ray binaries may have transient disks that are misaligned with respect to the binary orbit (Martin et al. 2009, 2011). These disks may be produced by the expulsion of equatorial material from a rapidly rotating Be star whose spin axis is misaligned with the binary rotation axis (e.g., Porter & Rivinus 2003).

There is both direct and indirect observational evidence for disk noncoplanarity. For widely separated stars in a binary, greater than 40 AU, a misaligned disk may occur because the stellar equatorial inclinations, based on spins, are observationally inferred to be misaligned with respect to the binary orbital planes (Hale 1994). The young binary system HK Tau provides direct evidence for noncoplanarity, since disks are observed around both

components with one disk edge-on and the other more face-on (Stapelfeldt et al. 1998). Recent ALMA observations by Jensen & Akeson (2014) suggest that its disks are mutually misaligned by more than 60° , although the plane of the binary orbit is not known. Strong mutual disk misalignment ($\sim 72^\circ$) has lately also been detected for the two circumstellar disks in V2434 Ori, a binary system in Orion (Williams et al. 2014). Less direct evidence comes from the existence of extra-solar planets whose orbits are tilted with respect to the spin axis of the central star (Albrecht et al. 2012; Winn & Fabrycky 2014). If the planets reside in binary star systems, this evidence suggests that these planets may have formed in disks that are misaligned with the binary orbital plane (e.g., Bate et al. 2010; Batygin 2012).

Test particles whose orbits are sufficiently inclined with respect to the plane of a circular orbit binary can undergo Kozai-Lidov (KL) oscillations (Kozai 1962; Lidov 1962). In these oscillations, the particle’s orbital inclination and eccentricity evolve in such a manner that inclination is exchanged for eccentricity. Due to this process, a test particle orbit that is initially circular can achieve a high eccentricity when it evolves to smaller inclination. For example, an initially circular orbit at an inclination of 60° achieves an eccentricity of about 0.75. Further extensions of this theory show that even stronger effects can occur for eccentric orbit binaries (Ford et al. 2000; Lithwick & Naoz 2011; Naoz et al. 2011, 2013a,b; Teyssandier et al. 2013; Li et al. 2014; Liu et al. 2015).

The KL effect for ballistic objects has been applied to a wide range of astronomical processes. These include inclinations of asteroids and irregular satellites (Kozai 1962; Nesvorný et al. 2003), high orbital eccentricities of some extra-solar planets and formation of hot Jupiters (Holman et al. 1997; Mazeh et al. 1997; Wu & Murray 2003; Takeda & Rasio 2005; Xiang-Gruess & Papaloizou 2013; Dawson & Chiang 2014; Dong et al. 2014; Petrovich 2015; Rice 2015), misalignment between an exoplanet’s

orbital axis and stellar spin axis (Storch et al. 2014, 2015), black hole mergers (Blaes et al. 2002; Miller & Hamilton 2002), the formation of close binary stars (Harrington 1968; Mazeh & Shaham 1979; Kiseleva et al. 1998; Fabrycky & Tremaine 2007), tidal disruption events (Chen et al. 2011), and the formation of Type Ia supernovae (Kushnir et al. 2013).

In a recent *Letter* (Martin et al. 2014b, hereafter Paper I), we showed in our Smoothed Particle Hydrodynamics (SPH) simulations that a fluid disk with pressure and viscosity that orbits a member of a binary can also undergo global KL oscillations. In this paper, we explore this process in more detail by considering how it is affected by various disk and binary parameters. Following the approach of Paper I, we attempt to relate the properties of disk KL oscillations to the properties of KL particle oscillations.

The outline of the paper is as follows. In Section 2 we describe the properties of particle orbits in binaries. The parameters of the particle orbits and the binaries are chosen to be similar to those of the disk simulations. In Section 3 we describe the results of SPH simulations for a range of initial particle numbers, disk viscosities, disk aspect ratios, initial density profiles (including changes to initial inner and outer disk radii), initial disk inclinations, binary mass ratios, and binary eccentricities. Section 4 contains the discussion and summary.

2. KL cycle of a test particle

As discussed in Paper I, the properties of a fluid disk undergoing KL oscillations are related to the properties of test (massless) particles undergoing KL oscillations that orbit at similar radii. In both the disk and test particle cases, the inclination and eccentricity are periodically exchanged. However, there are some fundamental differences. The period of a test particle oscillation varies with distance from the central object. In the case of a disk

that is subject to pressure and viscous forces, the oscillations are global (i.e., the period is the same over all radii) and subject to damping by dissipation, unlike the test particle case. The global disk oscillation frequency is expected to involve an angular momentum weighted average of the test particle oscillation frequencies (Equation (4) of Paper I). Before considering the disk oscillations, we describe in this section the behavior of test particle orbits. We apply binary parameters that are similar to those we adopt for the disk simulations described in Section 3.

We consider ballistic particle orbits around one component of a binary system. Each particle orbit is initially circular, but substantially inclined with respect to the orbital plane of the binary. If the binary orbit is circular, then over long timescales, the binary companion effectively acts as a uniform circular ring. Since this effective potential is time independent, the energy of the particle about the central mass is conserved. Thus, the semi-major axis a of the particle in a binary is nearly independent of time t , that is

$$a(t) \approx \text{constant}, \quad (1)$$

where the constant is determined by initial conditions. Because the time-averaged perturbing potential is axisymmetric, the component of the angular momentum of the particle that is perpendicular to the binary orbital plane is approximately conserved over long timescales. From this conservation principle and Equation (1) we have that

$$\sqrt{1 - e^2(t)} \cos(i(t)) \approx \text{constant}, \quad (2)$$

where the constant is determined by initial conditions, e is the orbital eccentricity of the particle, and i is the inclination of the particle orbit with respect to the binary orbital plane.

We denote the masses of the binary component objects as M_c and M_p , where M_c (M_p) is the mass of the central (perturbing) object to the particle orbit. Analytic calculations have determined that the KL oscillation period for a particle subject to the effect of a

binary in an eccentric orbit is approximately given by

$$\frac{\tau_{\text{KL}}}{P_{\text{b}}} \approx \frac{M_{\text{c}} + M_{\text{p}}}{M_{\text{p}}} \frac{P_{\text{b}}}{P} (1 - e_{\text{b}}^2)^{3/2} \quad (3)$$

(Holman et al. 1997; Innanen et al. 1997; Kiseleva et al. 1998), where $P = \sqrt{GM_{\text{c}}/a^3}$ is the orbital period of the particle with orbital semimajor axis a , $P_{\text{b}} = 2\pi/\Omega_{\text{b}}$ is the orbital period of the binary, e_{b} is the eccentricity of the binary orbit, and $\Omega_{\text{b}} = \sqrt{G(M_{\text{c}} + M_{\text{p}})/a_{\text{b}}^3}$ is the binary orbital frequency for binary semi-major axis a_{b} .

For the KL oscillations to occur, the initial inclination of the test particle orbit i_0 must satisfy the condition that $\cos^2(i_0) < \cos^2(i_{\text{cr}}) = 3/5$, where i_{cr} is the critical angle for KL oscillations. This condition requires that $39^\circ \lesssim i_0 \lesssim 141^\circ$. During the KL cycle, the inclination i of an initially circular prograde particle orbit ($i_0 < 90^\circ$) oscillates between the initial value i_0 and the critical angle $i_{\text{cr}} \simeq 39^\circ$, while the eccentricity oscillates between $e_{\text{min}} = 0$ and the maximum value of

$$e_{\text{max}} = \sqrt{1 - \frac{5}{3}\cos^2(i_0)}, \quad (4)$$

that is achieved for $i = i_{\text{cr}}$, which follows from Equation (2) with the right-hand side constant value of $\cos(i_0)$ (e.g., Innanen et al. 1997).

For an eccentric binary orbit, the vertical component of a particle’s angular momentum is not conserved. Equation (2) breaks down over long timescales and the maximum eccentricity of the particle can approach unity (Ford et al. 2000; Lithwick & Naoz 2011; Naoz et al. 2011, 2013a,b; Liu et al. 2015). The orbit can flip its orientation from prograde to retrograde with respect to the binary. This flip occurs as the orbit passes through a radial state ($e = 1$). In passing through a nearly radial orbit, the particle may collide with the central object.

In our numerical calculations, we compute the eccentricity of a test particle with coordinates $\mathbf{r}(t)$ by considering its specific angular momentum $\mathbf{j}(t)$ relative to the disk

central object at position $\mathbf{r}_c(t)$,

$$\mathbf{j}(t) = (\mathbf{r} - \mathbf{r}_c) \times (\dot{\mathbf{r}} - \dot{\mathbf{r}}_c), \quad (5)$$

where the dot denotes differentiation in time. The relative specific energy of the particle is

$$E(t) = \frac{1}{2}|\dot{\mathbf{r}} - \dot{\mathbf{r}}_c|^2 - \frac{GM_c}{|\mathbf{r} - \mathbf{r}_c|} \quad (6)$$

and thus its eccentricity is

$$e(t) = \sqrt{1 + \frac{2E|\mathbf{j}|^2}{(GM_c)^2}}. \quad (7)$$

The evolving inclination of the particle is

$$i(t) = \arccos\left(\frac{j_z}{|\mathbf{j}|}\right), \quad (8)$$

where j_z is the component of the angular momentum in Equation (5) that is perpendicular to the orbital plane of the binary.

Figure 1 plots the numerical results for a test particle undergoing KL oscillations from simple three-body simulations. The upper and lower rows show the evolution of the particle’s orbital eccentricity and inclination, respectively. We investigate the effects of changes to four system parameters: the initial orbit inclination i_0 , the initial orbital radius of the particle r_0 , the binary mass ratio M_p/M_c , and the binary eccentricity e_b . In all cases the initial orbital eccentricity of the particle is taken to be zero, $e_0 = 0$. Each column of the figure corresponds to runs where we vary one of these parameters and fix the other three at fiducial (reference standard) values. The fiducial parameters that we adopt for this figure are $i_0 = 60^\circ$, $r_0 = 0.2a_b$, $e_b = 0$, and $M_p/M_c = 1$. The fiducial value of r_0 is chosen as a characteristic radius that typically lies within the disks that we simulate in Section 3.

The left hand panels show that when the orbit of the particle is highly inclined (well above critical KL angle i_{cr} ; see the green and blue lines), the KL cycle period is relatively insensitive to inclination, as expected by Equation (3) that has no dependence

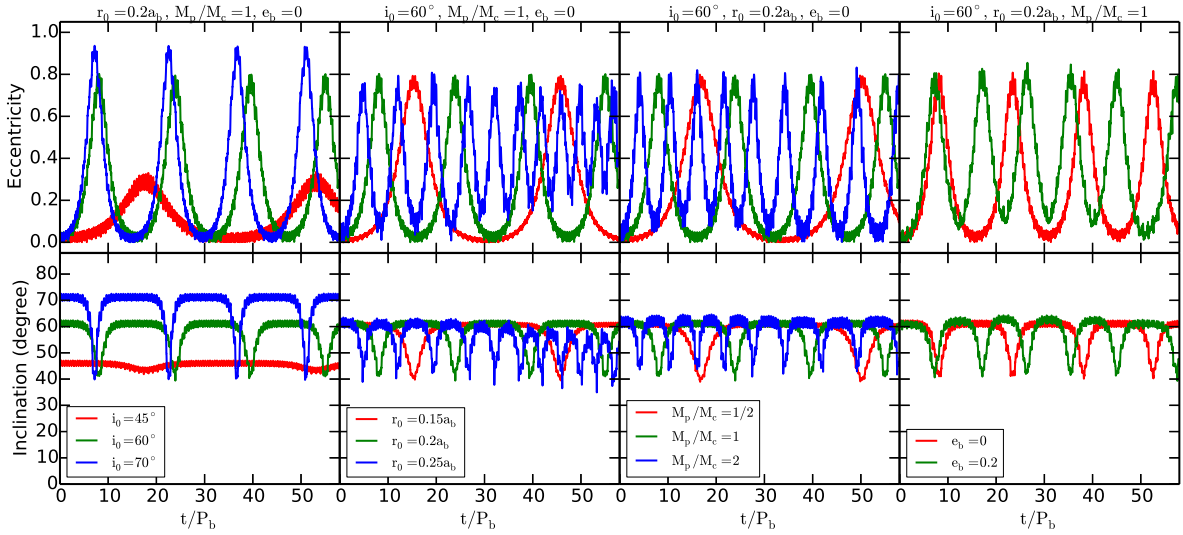


Fig. 1.— Eccentricity (upper row) and inclination (bottom row) evolution of a test particle for different values of the initial orbital inclination i_0 , initial orbital radius r_0 , binary mass ratio M_p/M_c , and binary eccentricity e_b . The binary orbit has a semi-major axis of a_b . Time is in units of binary orbital period P_b . These results are obtained from three-body numerical simulations. (Color online)

on inclination. The simulated period is sometimes close to that predicted by Equation (3). For $i_0 = 70^\circ$ (blue line), the eccentricity oscillation has $e_{\max} \simeq 0.93$ and $\tau_{\text{KL}} \simeq 15P_b$, while Equations (3) and (4) predict that $e_{\max} = 0.90$ and $\tau_{\text{KL}} = 16P_b$. When the initial orbital tilt is just above the critical KL angle, the KL cycle period given by Equation (3) becomes less accurate. For $i_0 = 45^\circ$ (red line), the period from the simulation is $\tau_{\text{KL}} \simeq 33P_b$, which is more than twice the analytical value.

The second column shows the effect of changing the initial orbital radius of the particle r_0 . The KL periods for $r_0 = 0.15a_b$, $0.2a_b$, and $0.25a_b$ are $\sim 30P_b$, $\sim 15P_b$, and $\sim 9P_b$, respectively. These values agree well (within $\sim 25\%$) with the predictions of Equation (3) that scales as $\tau_{\text{KL}} \propto r_0^{-3/2}$ and produces KL periods of $24P_b$, $16P_b$, and $11P_b$, respectively. Note that with $r_0 = 0.25a_b$, the KL cycle period becomes shorter and the oscillation amplitude is reduced at later time (e_{\min} does not reach zero). This is likely because at this orbital radius, the perturbing potential from the companion is more significant. As a result, the stronger influence makes the analytic description as a secular (gradual) effect less accurate and causes the oscillations to be irregular.

The effect of varying the binary mass ratio is shown in the third column. Equation (3) predicts that $\tau_{\text{KL}}/P_b \propto (M_c/M_p + 1)^{1/2}(M_c/M_p)^{1/2}$ such that $\tau_{\text{KL}} = 10P_b$, $16P_b$, and $27P_b$ for binary mass ratios $M_p/M_c = 2$, 1 , and $1/2$, respectively. The results of the numerical simulations give us $\tau_{\text{KL}} = 7P_b$, $15P_b$, and $32P_b$. The agreement is then within about 30%.

In the fourth column, we show the effect of varying the binary eccentricity. As discussed above, previous studies have shown that for eccentric orbit binaries, the maximum eccentricity can grow beyond e_{\max} given by Equation (4) and the maximum inclination can grow above the initial value of i_0 . As expected, for a somewhat higher binary eccentricity $e_b = 0.2$ (green lines), the maximum and minimum particle eccentricity sometimes increases somewhat in each KL oscillation. The oscillation period is shorter than in the circular case,

as predicted by Equation (3), since the companion object interacts more strongly with the particle at binary periastron. According to Equation (3), for $e_b = 0.2$, the KL oscillation period is approximately $14P_b$, whereas the numerically determined period in Figure 1 is about $10P_b$. Therefore, the reduction in the KL oscillation period due to binary orbital eccentricity is somewhat more severe than what is predicted analytically .

3. KL cycle of a hydrodynamic disk

In this section, we describe the KL cycles of three-dimensional hydrodynamic disks. We use the SPH code PHANTOM (Lodato & Price 2010; Price & Federrath 2010; Nixon 2012; Nixon & King 2012; Price 2012; Nixon et al. 2013). The disk is initially circular, centered around the binary component of mass M_c , and subject to perturbations by the other binary component of mass M_p . The disk orbital plane is initially misaligned with respect to the binary orbital plane. The disk initially extends from radius r_{in} to radius r_{out} . The inner boundary of the simulated region is set to the disk initial inner disk radius r_{in} . As particles move to $r \leq r_{\text{in}}$, they are removed from the simulation. We also impose an inner boundary radius around the perturbing companion, since some disk mass can be transferred to that component. The PHANTOM code adopts cubic spline kernel as the smoothing kernel. The softening length in the gravitational force is taken to be the same as the smoothing length. The number of neighbors is roughly constant at $N_{\text{neigh}} \approx 58$.

We define a certain set of fiducial (reference) model parameters. The disk is locally isothermal with sound speed $c_s \propto r^{-3/4}$ and disk aspect ratio $H/r = 0.035$ at the initial inner disk radius r_{in} . These parameters allow both α and the smoothing length $\langle h \rangle / H$ to be constant throughout the disk radius (Lodato & Pringle 2007). We employ an explicit accretion disk viscosity which corresponds to an approximately constant α parameter (Shakura & Sunyaev 1973) over the disk (see Lodato & Price 2010). The viscous stresses

include a nonlinear term with a coefficient $\beta_{\text{AV}} = 2$ (AV stands for artificial viscosity) that suppresses interparticle penetration, as is standard in SPH codes. The fiducial binary mass ratio is unity and the binary orbital eccentricity is zero (circular orbit). This fiducial setup is similar to that presented in Paper I. The only difference is that the initial number of particles in the fiducial model is set to $N = 3 \times 10^5$, while Paper I used $N = 1 \times 10^6$. The lower value adopted here reduces computational overhead in carrying out the various simulations, while providing results that are well converged in N , as we discuss below.

Table 1 lists the simulation parameters. We consider several models whose parameters deviate from the fiducial model, but not all combinations of parameters were simulated. Instead, we consider variations of one parameter with all others fixed at the fiducial values, as we did for particle orbits in Figure 1. For different mass ratios, we also adjust the initial inner and outer disk radii. We scale the initial disk inner radius from the central binary component by a factor of $(M_c/(M_c + M_p))^{1/3}$. As discussed above, the accretion radius of the central object is taken to be the same as the initial inner disk radius. The inner boundary condition is that any SPH particle that goes inside accretion radius is removed from the simulation. The inner boundary radius of the perturbing component is set to $r_{\text{in}}(M_p/M_c)^{1/3}$. The initial disk outer radius r_{out} is chosen to be that of a tidally truncated disk in a coplanar binary (Paczynski 1977). Thus, when we change the mass ratio of the binary, we also change the initial disk outer radius. However, in a misaligned binary the tidal torque on the disk is weakened and the disk can expand somewhat beyond this radius (Lubow, Martin & Nixon 2015). We ignore the effects of disk self-gravity in the simulations presented here. That means the disk does not feel its own gravity, but the stars can feel it. We set the ratio of the initial disk mass to the binary total mass to a very low value of 0.1% such that the binary orbit is hardly affected by disk’s gravity. This mass corresponds to a large initial Toomre Q of ~ 30 . We will devote a separate paper to studying the effects of higher disk mass and stronger self-gravity.

Table 1. Parameters of the SPH simulations for Binary Systems with Semi-major Axis of a_b

Binary and Disk parameters	Symbol	Fiducial Value	Values
Mass ratio of binary components	M_p/M_c	1	[0.25, 0.5, 1, 2]
Binary orbital eccentricity	e_b	0	[0, 0.2, 0.5]
Initial number of particles	$N/10^5$	3	[2, 3, 5, 10]
Initial disk mass	$M_{\text{disk}}/(M_c + M_p)$	0.001	0.001
Initial disk outer radius	r_{out}/a_b	0.25	[0.15, 0.25]
Initial disk inner radius	r_{in}/a_b	0.025	[0.015, 0.02, 0.025]
Mass accretion radius	r_{acc}/a_b	0.025	[0.015, 0.02, 0.025]
Disk viscosity parameter	α	0.1	[0.01, 0.1]
Disk aspect ratio	$H/r (r = r_{\text{in}})$	0.035	[0.02, 0.035, 0.05, 0.065]
Initial disk surface density profile $\Sigma \propto r^{-\gamma}$	γ	1.5	[0.5, 1.0, 1.5]
Initial disk inclination	i_0	60°	[45° , 50° , 55° , 60°]

In post-processing the simulations, we compute the orbital eccentricity and inclination for each particle using its position and velocity information according to Equations (7) and (8). We divide the disk into 100 radial bins and calculate the mean properties of the particles within each bin, such as the inclination and eccentricity. The properties of the particles in these radial bins are not fully independent of each other because the disk is generally eccentric. Particles residing one bin follow streamlines that cover other nearby bins. Therefore, some correlation of mean properties occurs in nearby bins. In most of our analysis, we apply fixed radial bins that are fairly widely separated to reduce these correlation effects. An alternative approach is to apply bins based on particle semi-major axis a . We have found that binning in r and a give similar results for most of our analysis and so we generally report results with bins in r for simplicity. For the determination of disk warping, however, we adopt bins based on particle semi-major axis, as described later.

The KL period of a test particle (Equation (3)) depends on the particle’s orbital radius. Following Paper I, we determine an analytic estimate of the KL global period of a disk by taking an angular momentum weighted average involving the local KL period of particle orbits as follows

$$\langle \tau_{\text{KL}} \rangle \approx \frac{\int_{r_{\text{in}}}^{r_{\text{out}}} \Sigma r^3 \sqrt{\frac{GM_c}{r^3}} dr}{\int_{r_{\text{in}}}^{r_{\text{out}}} \tau_{\text{KL}}^{-1} \Sigma r^3 \sqrt{\frac{GM_c}{r^3}} dr}, \quad (9)$$

where τ_{KL} in the denominator is given by Equation (3). This estimate is equivalent to determining the disk global precession frequency as the integrated torque divided by the total disk angular momentum. This estimate is crude because we apply the angular momentum of circular orbits, while the disk is generally eccentric. In addition, the analytic particle orbit period in Equation (3) is itself somewhat approximate, as we found in Section 2.

Figure 2 shows the evolution of the disk eccentricity and inclination at three different radii in the disk for various initial numbers of SPH particles. In this figure and following

similar figures, disk quantities are taken from three individual radial bins spanning 0.1 , 0.2 and $0.3a_b$, respectively. Also, we plot results up to a time of $t = 28P_b$. At this time, the disk has typically lost 90% of its initial particles. Most of the lost particles are accreted onto the central object. A small fraction of the particles are ejected from the disk, typically less than 10%. Most of ejected particles are accreted onto the companion and others remain in a circumbinary orbit. From Figure 2, we see that the effect of the numerical resolution on the disk KL mechanism is in general quite small, especially for the first two cycles. Although the cycle period at later times in the low resolution run is slightly shorter than that in high resolution run, all the curves damp to nearly the same level of eccentricity $e \simeq 0.2$ and inclination $i \simeq 28^\circ$ at a time $t = 28P_b$. Given this insensitivity of the overall disk KL cycle pattern to the numerical resolution, we adopt $N = 3 \times 10^5$ as the fiducial value that we use throughout the rest of the paper.

Figure 2 shows some differences from the test particle simulation results in Figure 1. We consider how Equations (1) and (2) might apply to a disk. We may expect a and e to represent a measure of the disk’s global semi-major axis and eccentricity, respectively, at some representative radius in the disk, such as the $r = 0.2a_b$ that we applied in Figure 1. Locally, a disk can transport angular momentum through waves and viscous torques. However, globally the vertical (perpendicular to the binary orbit plane) component of the disk angular momentum is conserved in the presence of an axisymmetric ring, apart from losses due to particles leaving the disk. On the other hand, the disk can dissipate energy, unlike the case of test particles. Therefore, the evolution of the disk is expected to depart from that of test particles, as given by Equations (1) and (2). In Figure 2, we see that the KL oscillations in the fluid case undergo damping in which the maxima of eccentricity decrease in time. In addition, the eccentricity minima do not drop to zero as in the particle case. The inclination drops below the minimum tilt of 39° for test particle oscillations. After the KL oscillations substantially damp, there is a significant residual disk eccentricity

$e \sim 0.2$.

The disk viscous timescale is estimated from Equation (18') of Lynden-Bell & Pringle (1974) as $t_v \sim r^2/(12\nu) \sim 20P_b$ for the fiducial model at $r = 0.25a_b$. We have also verified that the disk density evolution of the fiducial model roughly follows the results obtained from a 1D viscous disk model (omits pressure effects) (e.g., Lynden-Bell & Pringle 1974) for the same initial disk profile and level of viscosity. Therefore, over the course of the simulations, we expect the density profile to evolve from the initial one.

The first peak value of the eccentricity seen in the upper row of the plot $e \simeq 0.70$ is approximately consistent with the test particle results shown in Figure 1 for maximum $e \simeq 0.78$ with an initial tilt of 60° , although the test particles have a somewhat shorter KL period.

Figure 3 shows the effects of the disk viscosity on the KL mechanism. For lower viscosity (red curve; $\alpha = 0.01$), the time at which the first eccentricity cycle peaks is basically unaffected. However, both the eccentricity and the inclination damp at a lower rate because the disk is less dissipative. For $\alpha = 0.01$ at later times, the midpoints of the inclination KL oscillations settle to a tilt that is near the critical value of 39° for KL particle oscillations. Note that there is a substantial remnant disk eccentricity $e \sim 0.3$ after the KL oscillations significantly damp. The bottom panel of the figure plots the expected KL oscillation periods based on Equation (9). The estimated period is $\sim 15P_b$ that is to be compared with the period obtained in the SPH simulations (upper panel) of $\sim 7P_b$. The agreement is crude (factor of 2), likely for reasons noted below Equation (9).

The evolution of the disk eccentricity and inclination are well coordinated across different radii of the disk, as is evident from the similarity of the eccentricity and inclination curves across different radii in Figures 2 and 3. Figure 4 shows an edge-on view of the fiducial disk at $t = 0$ (left panel) and at $t = 13P_b$ (right panel) when the line of nodes

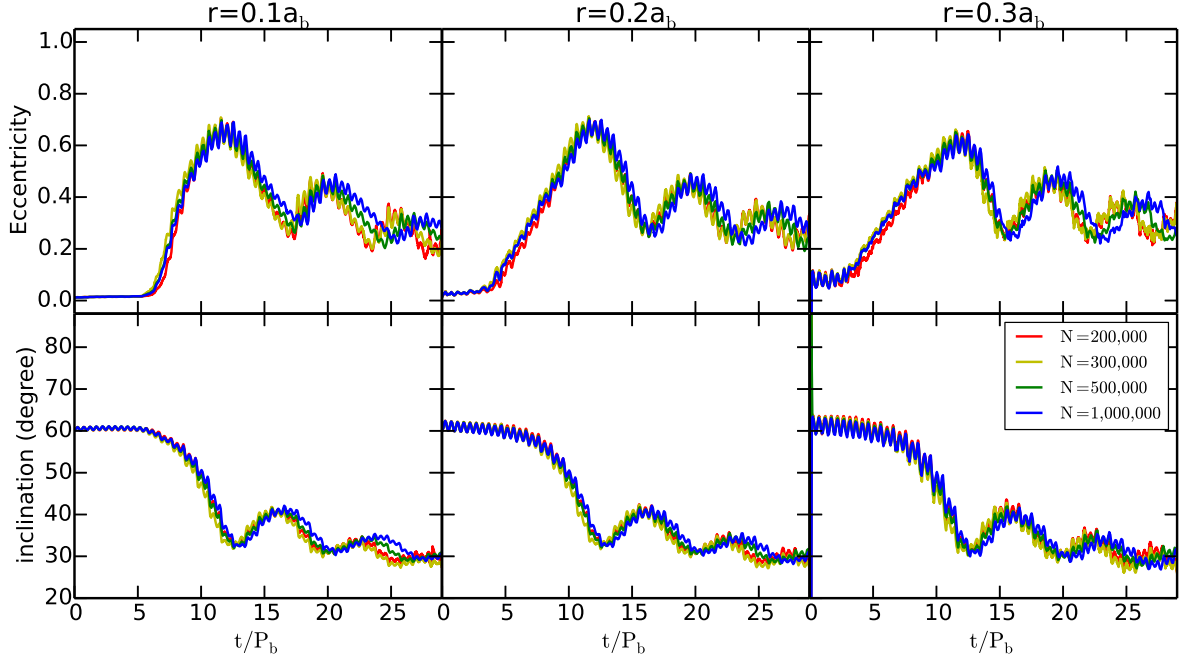


Fig. 2.— Eccentricity (upper row) and inclination (bottom row) evolution of the disk at three different radii from the central star for different initial numbers of particles. a_b is the binary semimajor axis and P_b is the binary orbital period. The other parameter values are given in the third column of Table 1. (color online)

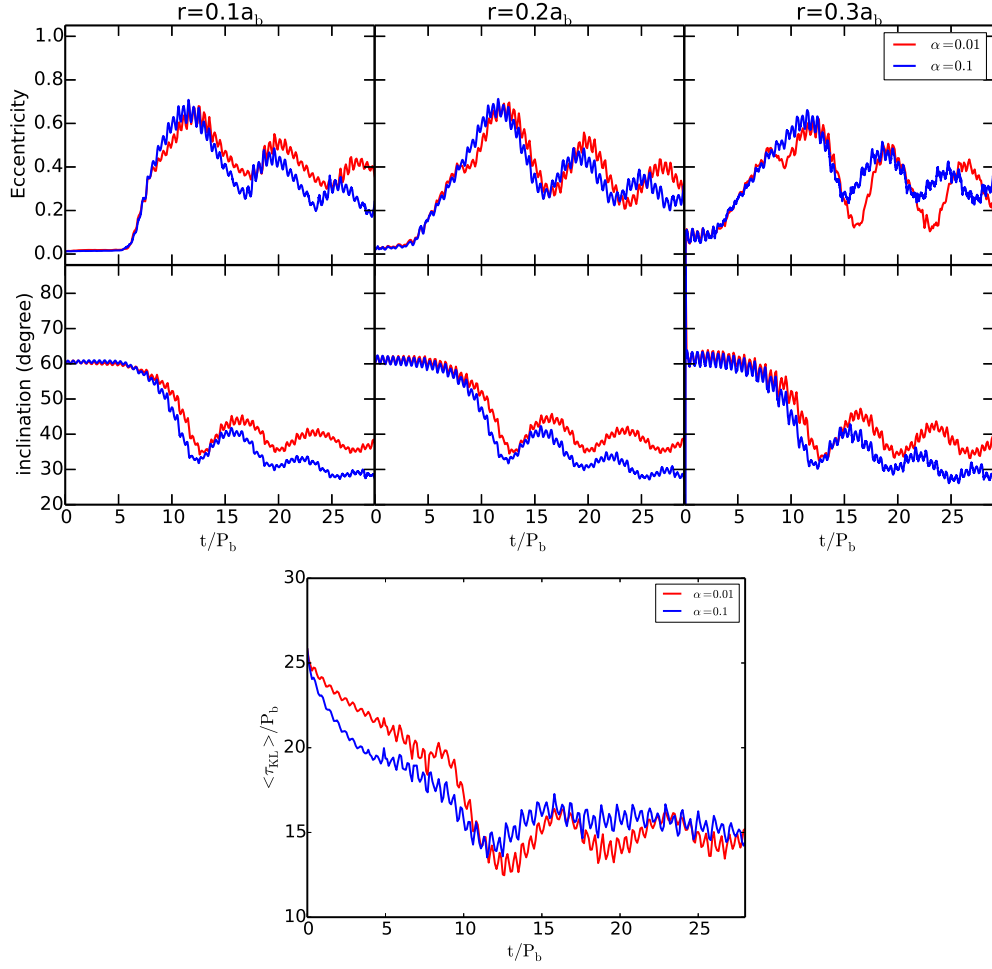


Fig. 3.— The upper figure is similar to Figure 2, but showing the effect of varying the disk viscosity parameter α . The lower figure shows the estimated disk KL period as a function of time (according to Equation (9)). (color online)

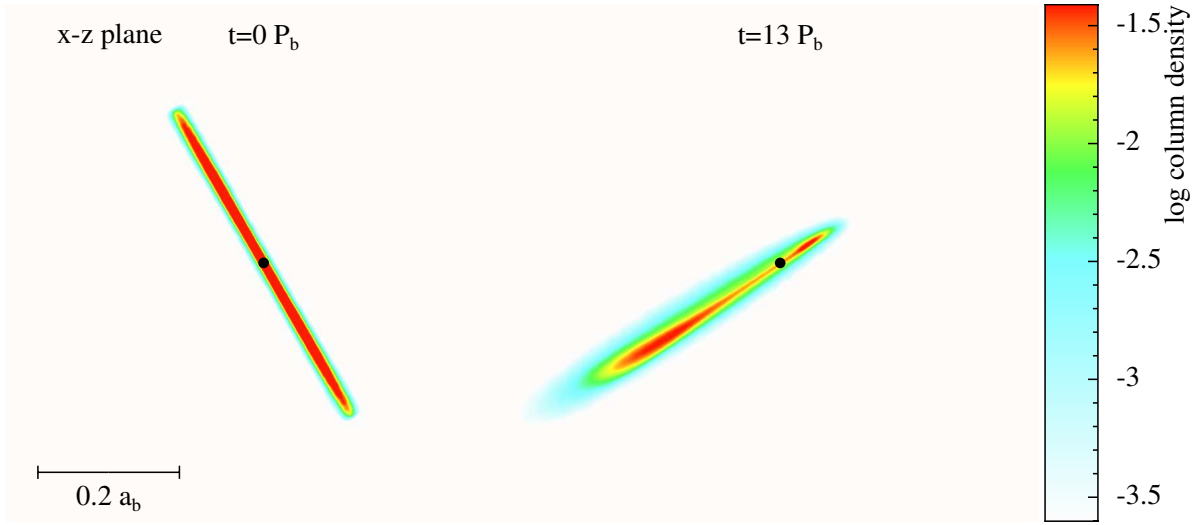


Fig. 4.— View of the fiducial disk toward the $x - z$ plane at times of 0 (left) and $13 P_b$ (right). The binary orbit is in the $x - y$ plane (i.e., the perturbing object moves into and out of the page). The central mass is denoted by the black dot. The color coding is for the logarithm base 10 of the column density (i.e., density integrated along the line of sight) in units of $(M_c + M_p)/a_b^2$. (Color online)

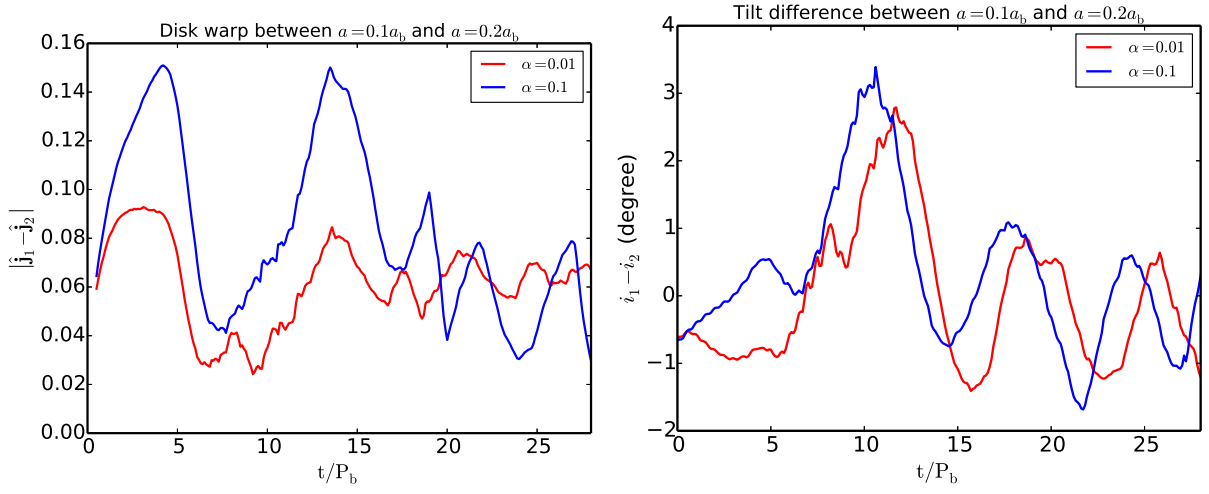


Fig. 5.— Left panel: the magnitude of the difference between the average disk angular momentum unit vectors for particles that lie in narrow bins of semi-major axis values centered on $a = 0.1a_b$ and $a = 0.2a_b$, averaged in time over one binary orbit, plotted as a function of time for runs in Figure 3. Right panel: the difference between average disk tilts for particles in narrow bins of semi-major axis values centered on $a = 0.1a_b$ and $a = 0.2a_b$, averaged in time over one binary orbit, plotted as a function of time for runs in Figure 3.

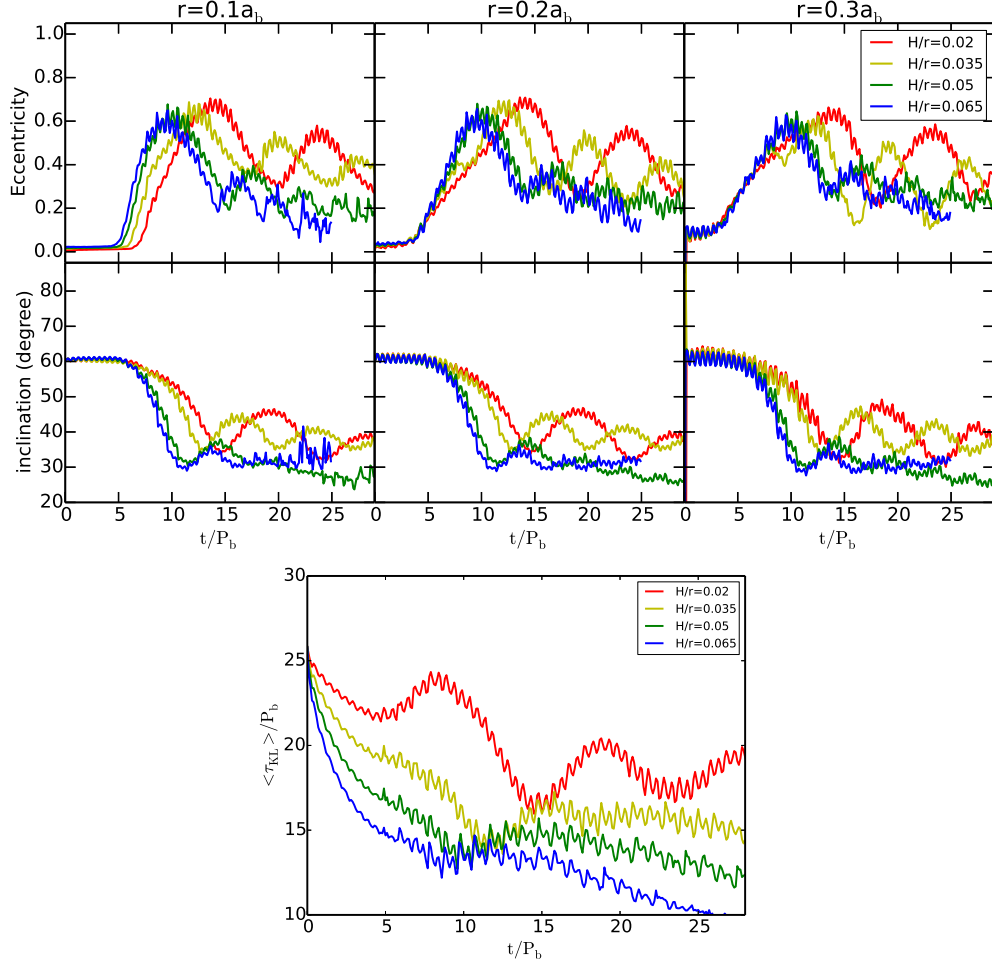


Fig. 6.— Similar to Figure 3, but showing the effect of varying the initial disk aspect ratio.
(color online)

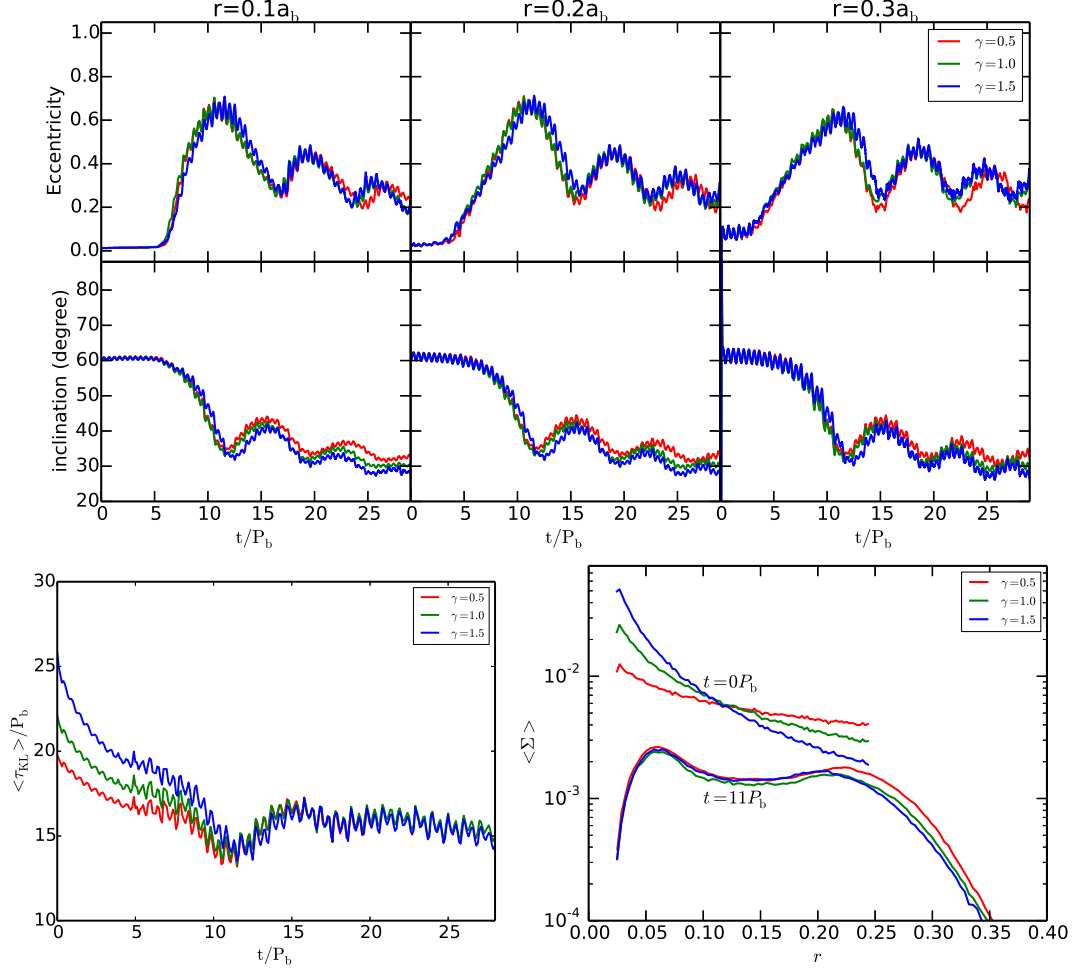


Fig. 7.— Similar to Figure 3, but showing the effect of varying the initial disk surface density profile. The lower right figure plots the azimuthally averaged surface density profiles at $t = 0P_b$ and $t = 11P_b$. The surface density is in units of $(M_c + M_p)/a_b^2$ and r is in units of a_b . (color online)

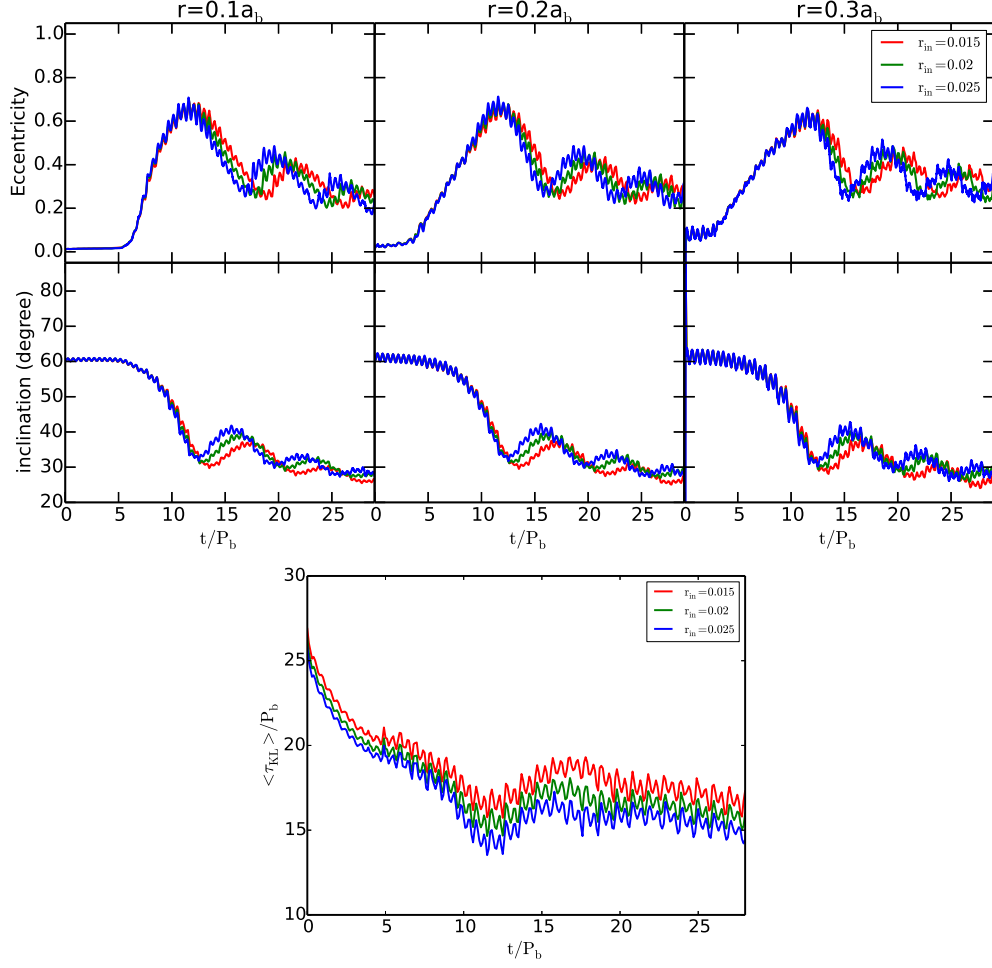


Fig. 8.— Similar to Figure 3, but showing the effect of varying the initial disk inner radius.
(color online)

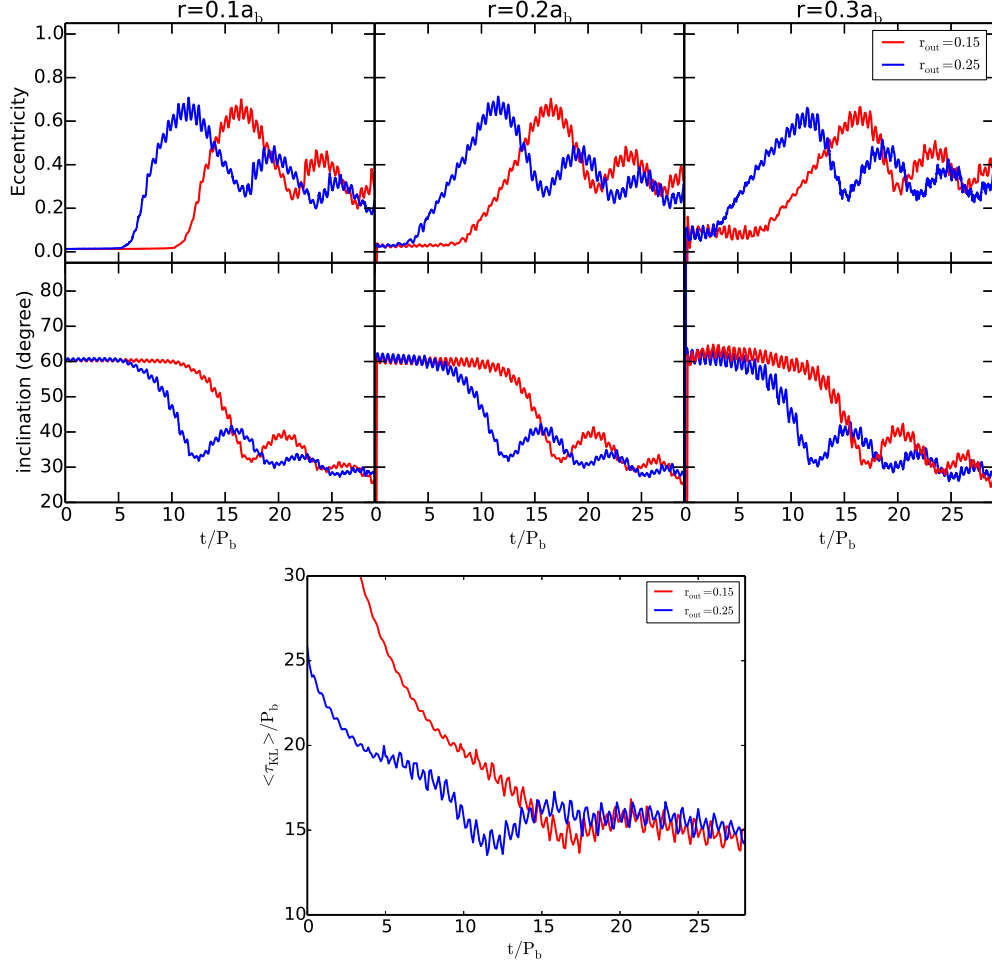


Fig. 9.— Similar to Figure 3, but showing the effect of varying the initial disk outer radius.
(color online)

has rotated by about 180° . This figure shows that the disk remains fairly flat, but quite lopsided, after substantial nodal and KL phase oscillation changes.

We consider how inclination is radially communicated across the a disk. A KL disk undergoes tilt oscillations, along with nodal precession. A disk that is in good radial communication would be expected to remain nearly flat, that is, have a small degree of warping. The disk warping is often measured by $r\partial_r\boldsymbol{\ell}$ where $\boldsymbol{\ell}$ is a unit vector that lies perpendicular to the local disk orbital plane. In the application to our simulation results, $\boldsymbol{\ell}(r)$ would be determined by the average value of $\boldsymbol{\ell}$ for particles in a narrow radial bin centered on radius r . However, as noted above, there are artificial correlations in quantities such as $\boldsymbol{\ell}(r)$. The reason is that eccentric streamlines carry a single value of $\boldsymbol{\ell}$ and extend radially in the disk. A better measure of warping is $a\partial_a\boldsymbol{\ell}$ where $\boldsymbol{\ell}(a)$ is determined by the average value of $\boldsymbol{\ell}$ for particles whose semi-major axes lie in a narrow bin of size $3.5 \times 10^{-3}a_b$ centered about semi-major axis a . The reason for using a is that (noncrossing) streamlines in a fluid disk can be uniquely labeled by their a values. Therefore, $a\partial_a\boldsymbol{\ell}$ measures warping across streamlines.

As an approximate measure of disk warping, we compute

$$\delta\hat{j} = |\hat{\mathbf{j}}_2 - \hat{\mathbf{j}}_1|, \quad (10)$$

where $\hat{\mathbf{j}}_1$ and $\hat{\mathbf{j}}_2$ are the average of the disk unit angular momentum vectors in bins of particle semi-major axis centered on a_1 and a_2 , respectively, that are separated by a_1 apart. We choose these values to be $a_1 = 0.1a_b$ and $a_2 = 0.2a_b$. For the KL effect on test particles in a circular orbit binary, a is conserved (Equation (1)). By a time $\sim 10P_b$, the value of $\delta\hat{j}$ for test particles is of order unity, since the outer particle that begins on a circular orbit with $r_0 = a = 0.2a_b$ undergoes a substantial change in tilt, as seen in Figure 1, as well as substantial nodal precession.

Radial communication in a disk is diffusive for $\alpha > H/r$ and wave-like for $\alpha < H/r$.

In the diffusive regime, the degree of warping is estimated by equating the binary nodal precessional torque to the horizontal (parallel to the disk) component of viscous torque that involves the so-called ν_2 viscosity (Natarajan & Pringle 1998). The ν_2 effective viscosity owes its existence to the internal flows driven by pressure gradients and limited by (e.g. turbulent) viscosity, as described by Papaloizou & Pringle (1983). We roughly estimate then that the warping due to nodal precession is

$$\delta\hat{j} \simeq \lambda \sin(i) \alpha \left(\frac{\omega_p}{\Omega}\right) \left(\frac{r}{H}\right)^2, \quad (11)$$

where λ is a coefficient of order unity, Ω is the circular frequency at the disk radius $r = 0.2a_b$, and ω_p is the nodal precession frequency. We have estimated that $\lambda \sim 0.3$ by solving the 1D viscous warp evolution equation given by Equation (10) of King et al. (2013) for the conditions in the fiducial model that has $\omega_p \sim 0.04\Omega_b$ and find that $\delta\hat{j} \sim 0.1$, which is roughly similar in value to the plotted results in left panel of Figure 5 for $\alpha = 0.1$ (blue curve).

The lower viscosity $\alpha = 0.01$ case plotted in left panel Figure 5 lies in the wave-like regime. The communication is a consequence of radial pressure forces. In this simulation the radial sound crossing timescale is substantially shorter than the KL oscillation or nodal precessional timescale. We have that $r/(c_s P_{KL}) \sim 0.1$. As described in Paper 1, because this ratio is small the disk undergoes global rigid tilt oscillations (Larwood & Papaloizou 1997; Lubow & Ogilvie 2001). In this case, the level of warping (plotted as the red curve on the left panel of Figure 5) is similar to or weaker than in the viscous regime (blue curve).

The warping $\delta\hat{j}$ depends on the variation of both the disk tilt and direction of the line of nodes. It is affected by both nodal precession and KL disk tilt oscillations. We consider here the variations of only the disk tilt. The KL inclination oscillations can lead to variations in disk tilt across streamlines in the disk. These variations can be expected because the KL oscillation timescale varies with particle orbit period P and therefore with particle orbit

semi-major axis a . According to Equation (3), the KL oscillation period should differ by about a factor of ~ 3 in a change from $a = 0.1a_b$ to $a = 0.2a_b$. Radial communication via viscous and pressure effects as described above play a role in maintaining a constant tilt. As seen in the right panel of Figure 5, the change in tilt between $a = 0.1a_b$ and $a = 0.2a_b$ is small. The difference in tilt angles between them is typically less than 3° . This change is similar to the disk aspect ratio $H/r = 0.035 \simeq 2.0^\circ$, while the disk oscillates over a range of tilt angles $\simeq 20^\circ$. In comparing the right panel of Figure 5 with Figure 3, we see that tilt difference is phased with the KL cycle. When the disk inclination is minimum and eccentricity is maximum, the outer inclination i_2 (that has $a = 0.2a_b$) is smaller than the inner inclination i_1 (that has $a = 0.1a_b$).

The effect of varying the disk aspect ratio is shown in Figure 6. Most noticeably, as the disk aspect ratio decreases (from the blue curve to the red curve), the first disk KL cycle gets delayed to a later time. Because the kinematic viscosity ν varies with $(H/r)^2$, lower values of H/r lead to a slower disk expansion and therefore a weaker perturbation from the companion object. Lower ν values also lead to slower damping in both eccentricity and inclination. The bottom panel of the figure shows the expected KL oscillation periods based on Equation (9). As we saw in the case of Figure 3, the accuracy of this equation is only to about a factor of 2. Based on the bottom panel, the ratio of KL periods for $H/r = 0.065$ to $H/r = 0.02$ is about 1.3, while the ratio in the SPH simulations (upper panel) is about 1.5.

We present in Figure 7 three runs using different power-law indices for the initial disk surface density profile. The differences in the results for these three cases is found to be quite small. The bottom left panel of this figure shows that the expected KL periods based on Equation (9) are about the same after a time of about $10P_b$, as is in agreement with the SPH simulations in the upper panels. The bottom right panel shows that after initial adjustment, the density distributions are very similar.

In Figure 8, we show the effects of changing the disk inner radius. The first disk KL cycle does not seem to be affected by the location of the disk inner boundary. However, the cycle period does get slightly longer as the disk inner radius decreases. The bottom panel of this figure shows that the expected KL periods based on Equation (9) are in qualitative agreement with this trend. This effect is likely be the result of having more material located further from the companion, closer to the central object, resulting in weaker global perturbations.

Figure 9 shows the effects of changing the disk outer radius. With smaller initial disk outer radius, the disk initially responds more slowly since the perturbations from the companion object are weaker. Thus, the effect in this case is simply a time delay in the cycles. The bottom panel of this figure shows that the expected KL periods based on Equation (9) are in agreement with this description. The case with the smaller initial radius has an initial KL period that is much longer than for disk of large initial radius. By a time of $\sim 15P_b$, both cases have the nearly same KL periods, as seen in the SPH simulations results of the upper panels.

Figure 10 shows the effects of changing the initial disk inclination. As i_0 varies from 60° to 45° , the KL cycles occur at a progressively later time with a longer cycle period and smaller oscillation magnitude. This trend seems to be in line with the test particle results discussed in the previous section, where the KL oscillation period increased with decreasing inclination. Equation (4) predicts eccentricity maxima of 0.76, 0.67, and 0.56 for initial tilts of 60° , 55° , and 50° , respectively, while Figure 10 exhibits maximum e values during the first KL cycle of 0.7, 0.6, and 0.4. In the test particle case, for an initial tilt of $i_0 = 45^\circ$, the eccentricity can reach values of 0.4, based on Equation (4), or 0.3, based on simulations (top-left panel of Figure 1). However, for this initial inclination angle, the KL mechanism barely operates in the disk whereas it is still relatively strong in the test particle

runs (see the left column of Figure 1). Thus, the critical initial tilt angle for the onset of KL oscillations in a hydrodynamical disk is somewhat higher than for a test particle (39°). On the other hand, in the first disk KL cycle, the inclination can drop below 39° , which does not occur in the particle case.

Figure 11 demonstrates the effects of varying the binary mass ratio. For $M_p/M_c \leq 1$, a smaller mass ratio leads to a later occurrence of the KL cycle and also a longer cycle period (from the green curve to the red curve), which again is in line with the test particle results. The bottom panel of this figure shows that the expected KL periods based on Equation (9) at a time of $25P_b$ are about $30P_b$, $20P_b$, $15P_b$, and $7P_b$ for mass ratios of $1/4$, $1/2$, 1 , and 2 , respectively, whereas the SPH simulation results show $15P_b$, $11P_b$, $8P_b$, and $11P_b$. For both approaches for mass ratios less than or equal to unity, the KL period decreases with mass ratio, as expected. The period for the corresponding cases are again different by about a factor of 2. In the case where the perturbing companion is more massive with a mass ratio of 2, the period in the SPH simulation does not follow this trend and instead increases.

The effects of varying the binary eccentricity are shown in Figure 12. The initial disk outer radius is $r_{\text{out}} = 0.2a_b$ instead of the fiducial value of $0.25a_b$. This smaller initial disk outer radius was used because the increased binary eccentricity causes a stronger response in the disk and a smaller disk truncation radius, as is known to occur for the coplanar case (Artymowicz & Lubow 1994). Other parameters are set to their fiducial values. We do not plot the results for $e_b = 0.5$ at $r = 0.2a_b$ and $r = 0.3a_b$ because the disk is truncated within this radius due to the smaller periastron distance. The KL oscillation periods are about the same in the three cases, within about 10% of each other. The maximum eccentricities are also about the same in the three cases, as we found for test particles in Section 2. In the $e_b = 0.5$ case, the inclination decays to a value close to $i_{\text{cr}} = 39^\circ$, while the lower binary eccentricity cases decay to a smaller tilt angle.

4. Discussion and Summary

In this paper, we investigated the conditions under which KL oscillations can operate on a fluid disk, as was first described in Martin et al. (2014b). Such a disk undergoes a complicated evolution involving tilt and eccentricity oscillations, as well as the usual nodal and apsidal precession. We carried out this analysis by means of SPH simulations that include the effects of disk pressure and viscosity. We considered a range of disk viscosities (Figure 3), sound speeds (Figure 6), initial density profiles (Figures 7, 8, 9), initial inclinations (Figure 10), binary mass ratios (Figure 11), and binary eccentricities (Figure 12). We found that the KL effect generally operates over a range of disk and binary properties.

The general picture we have is that an initially circular circumstellar disk that is sufficiently inclined ($\sim 45^\circ - 135^\circ$) with respect to the orbit plane of a binary undergoes damped KL eccentricity and tilt oscillations. During these oscillations, the disk can develop substantial eccentricities, $e \gtrsim 0.5$. Once the KL oscillations have mostly damped, the disk achieves a tilt in the prograde disk case (initial tilt less than 90°) $i \simeq 39^\circ$ or somewhat smaller and an eccentricity of up to a few tenths. Over longer timescales, if the disk survives that long, we expect that the disk eccentricity will eventually damp (e.g., Ogilvie 2001) and the disk will become coplanar with the binary orbit plane (e.g., King et al. 2013) due to viscous effects.

The properties of KL disk oscillations are somewhat similar to the properties of KL test particle oscillations (Figure 1). In both cases, inclination and eccentricity are interchanged. The peak eccentricity achieved by a disk in the first KL oscillation is generally close to the eccentricity achieved by test particles for the same initial inclination. In addition, for smaller mass perturbers, the KL oscillations are slower for both test particles and disks (Figure 11).

However, there are some significant differences between a fluid disk and test particles. The KL oscillation frequency of test particles varies with particle orbit semi-major axis as $a^{3/2}$. On the other hand, a disk undergoes a large scale global oscillation with a small level of warping for typical parameters (Figures 4 and 5). For a circular orbit binary, the inclination of prograde test particle orbits relative to the binary orbit plane must be greater than the critical angle $i_{\text{cr}} = \arccos(\sqrt{3/5}) \simeq 39^\circ$ for KL oscillations to occur. In the case of a disk, we find that the minimum inclination angle appears to be somewhat larger ($\gtrsim 45^\circ$) (see Figure 10). For a circular orbit binary, the inclination of prograde test particle orbits oscillates between the initial value $i_0 > i_{\text{cr}}$ and i_{cr} . For the case of a disk, however, the oscillation can dip below i_{cr} (e.g., Figure 3). Therefore, even though a disk requires a larger tilt to operate than a test particle orbit, the disk oscillations can reach lower tilt angles.

Another major difference between test particles and disks is that disks can dissipate energy. As a result, the KL oscillations damp, but leave a residual disk eccentricity that we find to be typically a few tenths. We find that the damping rate depends on the level of disk viscosity (Figure 3). The disk eccentricities may also damp through a decay process involving a parametric instability (Papaloizou 2005a,b; Barker & Ogilvie 2014; Ogilvie & Barker 2014). Our simulations may not be capable of resolving this instability that occurs on scales smaller than the disk thickness. It is also possible that the initial KL oscillation damping involves shocks, since the streamlines may attempt to cross at high eccentricity. We have found indirect evidence for such effects in some simulations that we carried out with a low value of viscosity parameter β_{AV} . As mentioned in Section 3, this parameter is used in the SPH code to prevent interparticle penetration that artificially occurs in the code where shocks are present. For small values of β_{AV} , the SPH simulations displayed unphysical behavior, symptomatic of interparticle penetration. Over longer timescales in the post-KL oscillation phase, the disk is expected to eventually align with the binary orbit plane through viscous effects (e.g., King et al. 2013).

For an eccentric orbit binary, the KL test particle oscillations can reach to higher inclination angles than the initial tilt. Inclination angles can reach 90° and even higher, resulting flipping from prograde to retrograde orbits (Lithwick & Naoz 2011; Naoz et al. 2011, 2013a,b; Liu et al. 2015). In reaching 90° , the orbit becomes radial. KL disk oscillations cannot achieve a similar increased level of inclination (certainly not to eccentricity close to unity) because of dissipation.

In this paper, we have omitted the effects of disk self-gravity. Such effects may suppress KL oscillations for sufficiently massive disks (Batygin 2012; Martin et al. 2014b). We intend to describe the influence of self-gravity in a future paper.

Confirmation of the KL mechanism acting on a disk would come from an observation of an eccentric and misaligned disk in a binary system. The KL oscillations are applicable to binary systems on all scales. For example, the oscillations could play a role in planet formation and evolution around one component of a binary star. There is observational evidence that some exoplanets may be undergoing KL cycles in wide binaries (e.g. Wu & Murray 2003; Takeda & Rasio 2005). In future work, we plan to investigate the evolution of a planet–disk system that orbits around one component of a binary system in order to understand how these planets can form.

Be/X-ray binaries may also be influenced by the KL oscillations of a misaligned disk (Martin et al. 2014a,b). Be stars may form disks from material that is ejected from the equator of the rapidly rotating star (Lee, Osaki & Saio 1991; Hanuschik 1996; Carciofi 2011). Be/X-ray binaries contain a Be star with a rotation axis that is misaligned to that of the orbit of a companion neutron star (see Table 1 in Martin et al. 2011, for some observations). We found in our simulations that roughly 10% of the initial disk mass is captured by the companion object for the fiducial model. As a disk undergoes KL oscillations to maximum eccentricity, its apastron radius grows which allows this capture to

occur. This mass exchange may explain the so-called giant Type II outbursts as being due to the accretion of disk mass by the companion neutron star (Martin et al. 2014a).

Finally, the KL oscillations of a disk may also be relevant to SMBH binaries. It is possible that the circumbinary disk around a SMBH binary will be misaligned (e.g. Nixon et al. 2011a,b). Thus, as gas accretes inwards from the circumbinary disk, misaligned disks will form around each SMBH. These disks will be unstable to KL oscillations if the misalignment angle is sufficiently large. This effect could have implications for the subsequent disk evolution and star formation in these systems.

W.F. and S.H.L. acknowledge support from NASA grant NNX11AK61G. Computing resource supporting this work was provided by the institutional computing program at Los Alamos National Laboratory. We thank Daniel Price for providing the **PHANTOM** code for SPH simulations and **SPLASH** code (Price 2007) for data analysis and rendering of figures.

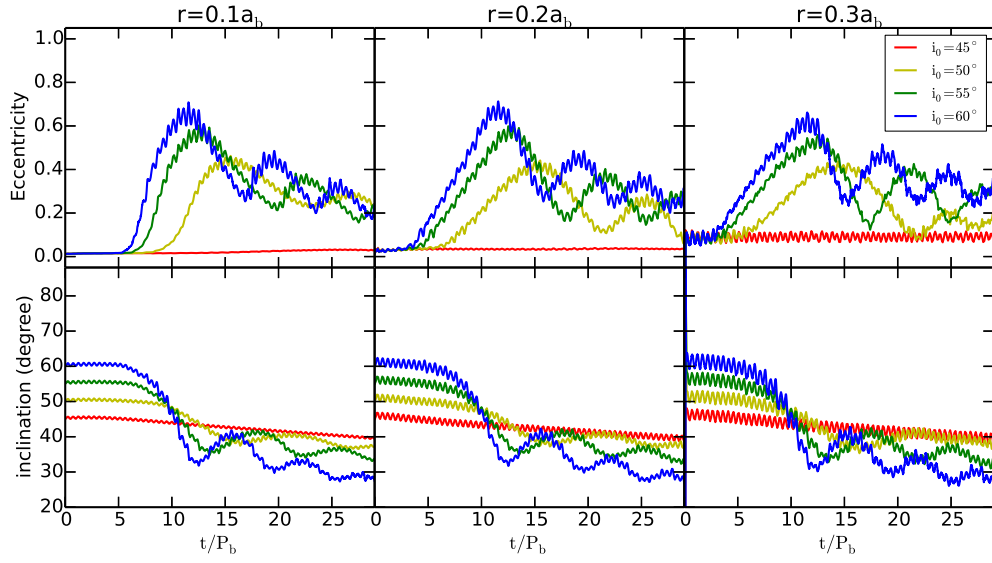


Fig. 10.— Similar to Figure 3, but showing the effect of varying the initial disk inclination angle. (color online)

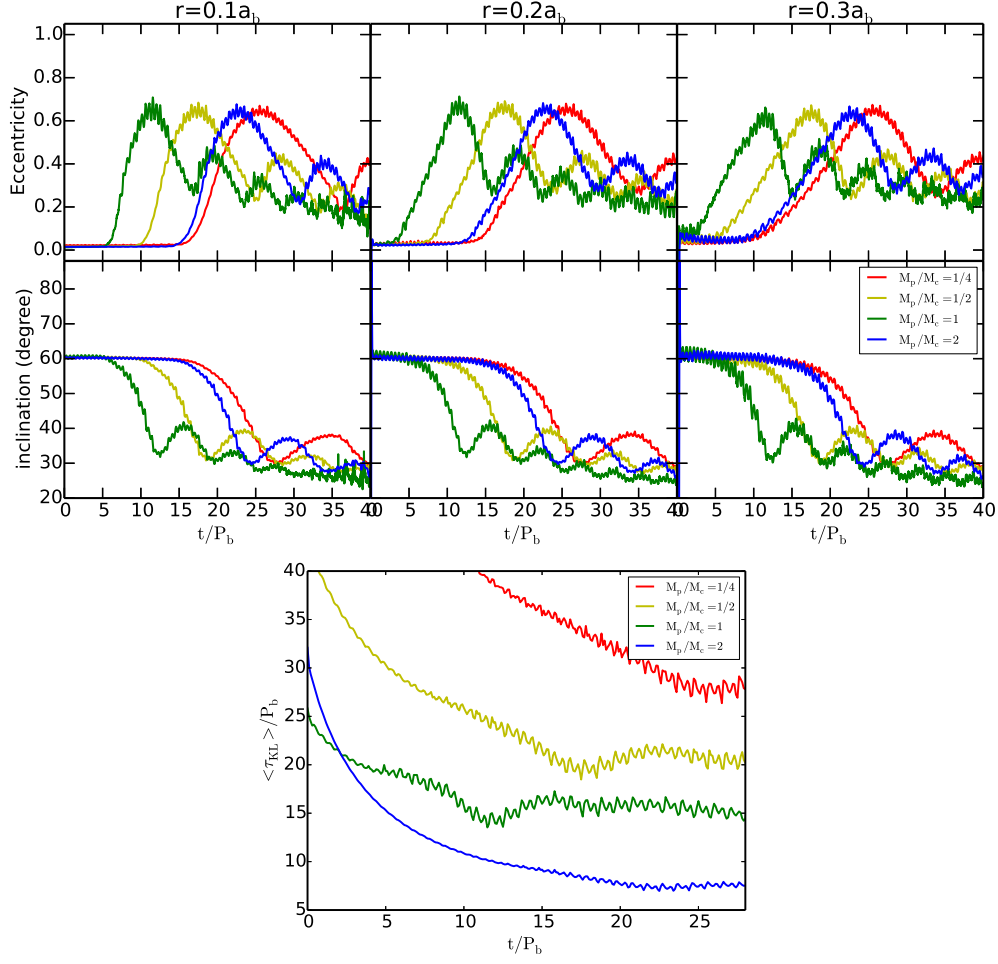


Fig. 11.— Similar to Figure 3, but showing the effect of varying the binary mass ratio. Note that here we show results up to $t = 40P_b$ in the upper figure. (color online)

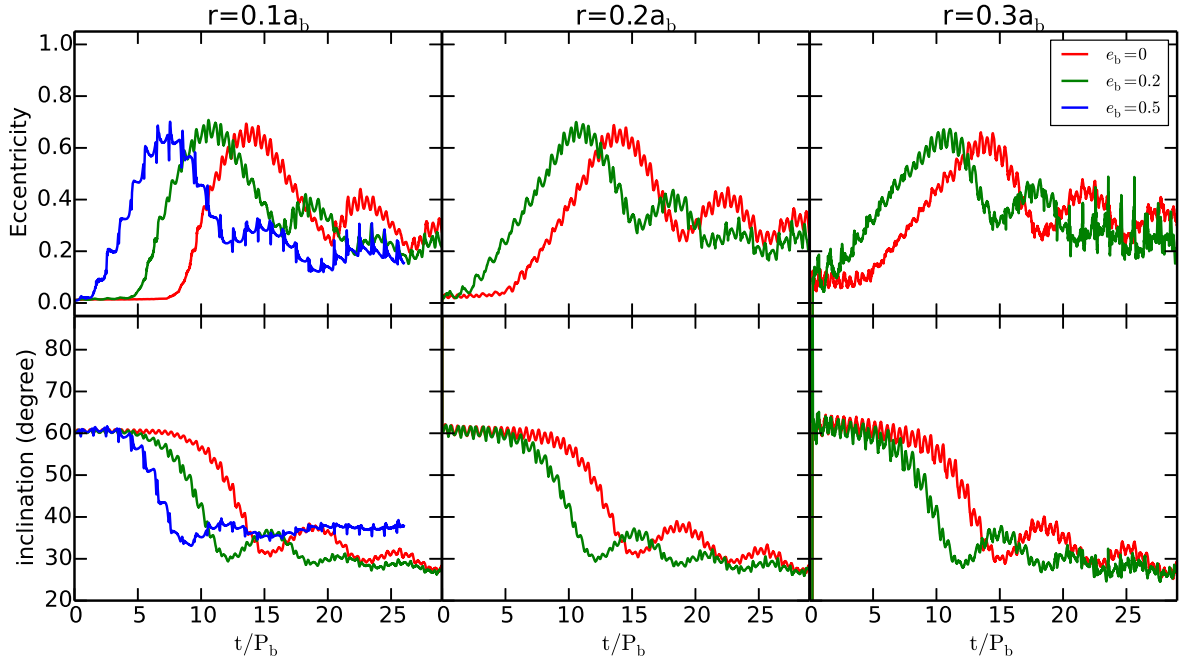


Fig. 12.— Similar to Figure 2, but showing the effect of varying the binary eccentricity.
(color online)

REFERENCES

- Artymowicz, P., & Lubow, S. H. 1994, *ApJ*, 421, 651
- Albrecht, S., Winn, J. N., Johnson, J. A., et al. 2012, *ApJ*, 757, 18
- Barker, A. J., & Ogilvie, G. I. 2014, *MNRAS*, 445, 2637
- Bate, M. R., Bonnell, I. A., Clarke, C. J., et al. 2000, *MNRAS*, 317, 773
- Bate, M. R., Lodato, G., & Pringle, J. E. 2010, *MNRAS*, 401, 1505
- Batygin, K. 2012, *Nature*, 491, 418
- Blaes, O., Lee, M. H., & Socrates, A. 2002, *ApJ*, 578, 775
- Bonnell, I. A., & Bate, M. R. 1994, *MNRAS*, 269, L45
- Carciofi, A. C. 2011, in *IAU Symp. 272, Active OB Stars: Structure, Evolution, Mass Loss, and Critical Limits*, ed. C. Neiner, G. Wade, G. Meynet, & G. Peters (Cambridge: Cambridge Univ. Press), 325
- Chen, X., Sesana, A., Madau, P., & Liu, F. K. 2011, *ApJ*, 729, 13
- Dawson, R. I. & Chiang, E. 2014, *Science*, 346, 212
- Dong, S., Katz, B., & Socrates, A. 2014, *ApJL*, 781, L5
- Fabrycky, D., & Tremaine, S. 2007, *ApJ*, 669, 1298
- Ford, E. B., Kozinsky, B., & Rasio, F. A. 2000, *ApJ*, 535, 385
- Hale, A. 1994, *AJ*, 107, 306
- Hanuschik, R. W. 1996, *A&A*, 308, 170

- Harrington, R. S. 1968, *AJ*, 73, 190
- Holman, M. J., Touma, J., & Tremaine, S. 1997, *Nature*, 386, 254
- Innanen, K. A., Zheng, J. Q., Mikkola, S., & Valtonen, M. J. 1997, *AJ*, 113, 1915
- Jensen, E. L. N. & Akeson, R. 2014, *Nature*, 511, 567
- King, A. R., & Pringle, J. E. 2006, *MNRAS*, 373, L90
- King, A. R., Livio, M., Lubow, S. H., & Pringle, J. E. 2013, *MNRAS*, 431, 2655
- Kiseleva, L. G., Eggleton, P. P., & Mikkola, S. 1998, *MNRAS*, 300, 292
- Kozai, Y. 1962, *AJ*, 67, 591
- Kushnir, D., Katz, B., Dong, S., Livne, E., & Fernández, R. 2013, *ApJL*, 778, L37
- Larwood, J. D., & Papaloizou, J. C. B. 1997, *MNRAS*, 285, 288
- Lee, U., Osaki, Y., & Saio, H. 1991, *MNRAS*, 250, 432
- Li, G., Naoz, S., Kocsis, B., & Loeb, A. 2014, *ApJ*, 785, 116
- Lidov, M. L. 1962, *P&SS*, 9, 719
- Lithwick, Y., & Naoz, S. 2011, *ApJ*, 742, 94
- Liu, B., Muñoz, D., & Lai, D. 2015, *MNRAS*, 447, 747
- Lodato, G., & Pringle, J. E. 2007, *MNRAS*, 381, 1287
- Lodato, G., & Price, D. J. 2010, *MNRAS*, 405, 1212
- Lubow, S. H., Martin, R. G., & Nixon, C. J. 2015, *ApJ*, 800, 96
- Lubow, S. H., & Ogilvie, G. I. 2000, *ApJ*, 538, 326

- Lubow, S. H., & Ogilvie, G. I. 2001, *ApJ*, 560, 997
- Lynden-Bell, D. & Pringle, J. E., *MNRAS*, 168, 603
- Martin R. G., Tout, C. A., & Pringle J. E. 2009, *MNRAS*, 397, 1563
- Martin R. G., Pringle J. E., Tout C. A., & Lubow S. H. 2011, *MNRAS*, 416, 2827
- Martin, R. G., Nixon, C., Armitage, P. J., Lubow, S. H., & Price, D. J. 2014a, *ApJL*, 790, L34
- Martin, R. G., Nixon, C., Lubow, S. H., et al. 2014b, *ApJ*, 792, L33
- Mazeh, T., Krymolowski, Y., & Rosenfeld, G. 1997, *ApJL*, 477, L103
- Mazeh, T., & Shaham, J. 1979, *A&A*, 77, 145
- Miller, M. C., & Hamilton, D. P. 2002, *ApJ*, 576, 894
- Naoz, S., Farr, W. M., Lithwick, Y., Rasio, F. A., & Teyssandier, J. 2011, *Nature*, 473, 187
- Naoz, S., Farr, W. M., Lithwick, Y., Rasio, F. A., & Teyssandier, J. 2013a, *MNRAS*, 431, 2155
- Naoz, S., Kocsis, B., Leob A., & Yunes, N. 2013b, *ApJ*, 773, 187
- Natarajan, P., & Pringle, J. E. 1998, *ApJL*, 506, L97
- Nesvorný, D., Alvarellos, J. L. A., Dones, L., & Levison, H. F. 2003, *AJ*, 126, 398
- Nixon, C. J., Cossins, P. J., King, A. R., Pringle, J. E. 2011a, *MNRAS*, 412, 1591
- Nixon, C. J., King, A. R., Pringle, J. E. 2011b, *MNRAS*, 417, L66
- Nixon, C. J. 2012, *MNRAS*, 423, 2597

- Nixon, C. J., & King, A. R. 2012, MNRAS, 421, 1201
- Nixon, C., King, A., & Price, D. 2013, MNRAS, 434, 1946
- Offner, S. S. R., Kratter, K. M., Matzner, C. D., Krumholz, M. R., & Klein, R. I. 2010, ApJ, 725, 1485
- Ogilvie, G. I. 2001, MNRAS, 325, 231
- Ogilvie, G. I., & Barker, A. J. 2014, MNRAS, 445, 2621
- Ogilvie, G. I., & Dubus, G. 2001, MNRAS, 320, 485
- Paczynski, B. 1977, ApJ, 216, 822
- Papaloizou, J. C. B. 2005a, A&A, 432, 743
- Papaloizou, J. C. B. 2005b, A&A, 432, 757
- Papaloizou, J. C. B., & Pringle, J. E. 1983, MNRAS, 202, 1181
- Papaloizou, J. C. B., & Terquem, C. 1995, MNRAS, 274, 987
- Petrovich, C. 2015, ApJ, 799, 27
- Porter, J. M., & Rivinius, T. 2003, PASP, 115, 1153
- Price, D. J. 2007, PASA, 24, 159
- Price, D. J., & Federrath, C. 2010, MNRAS, 406, 1659
- Price, D. J. 2012, JCoPh, 231, 759
- Pringle, J. E. 1996, MNRAS, 281, 357
- Rice, K. 2015, MNRAS, 448, 1729

- Storch, N., Kassandra, R. A., & Lai, D. 2014, *Science*, 345, 1317
- Storch, N., & Lai, D. 2015, *MNRAS*, 448, 1821
- Shakura, N. I., & Sunyaev, R. A., 1973, *A&A*, 24, 337
- Stapelfeldt, K. R., Krist, J. E., Ménard, F., et al. 1998, *ApJL*, 502, L65
- Takeda, G., & Rasio, F. A. 2005, *ApJ*, 627, 1001
- Teyssandier, J., Naoz, S., Lizarraga, I., & Rasio, F. A. 2013, *ApJ*, 779, 166
- Wijers, R. A. M. J., & Pringle, J. E. 1999, *MNRAS*, 308, 207
- Williams, J. P., Mann, R. K., Di Francesco, J., et al. 2014, *ApJ*, 796, 120
- Winn, J. N., & Fabrycky, D. C. 2014, *arXiv:1410.4199*
- Wu, Y., & Murray, N. 2003, *ApJ*, 589, 605
- Xiang-Gruess, M., & Papaloizou, J. C. B. 2013, *MNRAS*, 431, 1320